A novel experimental technique and its application to study the effects of particle density and flow submergence on bed particle saltation

Mohammad Amir, Vladimir Nikora & Matthew Witz

Published online: 24 Oct 2016.

Submit your article to this journal ↗

Article views: 359

View related articles ↗

View Crossmark data ↗

Research paper

A novel experimental technique and its application to study the effects of particle density and flow submergence on bed particle saltation

MOHAMMAD AMIR, Research Fellow, *School of Engineering, University of Aberdeen, Aberdeen, UK (currently Fluid Mechanics Development Engineer, Silixa Ltd, 230 Centennial Park, Centennial Avenue, Elstree, Hertfordshire, UK)*
Email: *mohammad.amir@silixa.com (author for correspondence)*

VLADIMIR NIKORA (IAHR Member), Professor, *School of Engineering, University of Aberdeen, Aberdeen, UK*
Email: *v.nikora@abdn.ac.uk*

MATTHEW WITZ, Honorary Research Fellow, *School of Engineering, University of Aberdeen, Aberdeen, UK (currently Subsea Engineer, Crondall Energy Subsea Ltd, Aberdeen, UK)*
Email: *m.witz@abdn.ac.uk*

ABSTRACT
A novel technique has been developed to measure bed particle flight durations and amplitudes using the impact data from the records of instantaneous pressure acting on multiple bed particles. It has the potential to measure many more particle jumps compared to other methods, thus generating records long enough for well-converged statistics of the variables of interest. The proposed technique has been validated with independent measurements by a tracking method using a four camera particle image velocimetry system. The application of this technique in a laboratory study revealed that probability distributions and statistical moments of flight durations and heights are strongly dependent on flow submergence and particle density.

Keywords: Open-channel flow; particle entrainment; particle flight durations; particle flight heights; pressure sensors; saltation; sediment particles

1 Introduction

Transport of bedload particles in water flows occurs in the form of sliding, rolling, saltation (e.g. Bagnold, 1977; Dey, 2014; Graf, 1984; Yalin, 1977) or their combinations (e.g. Ancey, Davison, Böhm, Jodeau, & Frey, 2008; Lajeunesse, Malverti, & Charru, 2010). The dominance of particular transport modes depends on many factors such as bed particle shape, density, size distribution, bed roughness, bed shear stress, and flow structure. The present paper focuses on the saltation mode that, although being recognized as a key transport mode, remains insufficiently understood. Most of the knowledge on particle saltation in water flows comes from the studies of Gordon, Carmichael, and Isackson (1972), Francis (1973), Abbott and Francis (1977), Fernandez-Luque and Van Beek (1976), Murphy and Hooshiari (1982), Hui and Hu (1991), Lee and Hsu (1994), Niño and Garcia (1994, 1998), Niño, Garcia, and Ayala (1994), Ancey, Bigillon, Frey, Lanier, and Ducret (2002), Ancey et al. (2008),

Lajeunesse et al. (2010), Bialik (2011), Ramesh, Kothyari, and Murugesan (2011), Campagnol et al. (2013), among others. These researchers used photographic techniques and numerical simulations to study the saltating trajectories and the corresponding heights, lengths, velocities, and accelerations of saltating particles.

Despite a fairly large number of works addressing the motion of saltating particles, the studies which have so far been conducted to explicitly investigate the effects of flow submergence on particle trajectories remain very limited. There is evidence, however, that flow submergence has an important control on turbulent structures in rough-bed flows (e.g. Cooper, Aberle, Koll, & Tait, 2013; Shvidchenko & Pender, 2001). As the size, energy, and spatial organization of the flow structures may influence the saltating motion of the particles, it is important to isolate the effect of flow submergence, representing turbulence features, from other effects (e.g. particle size, shape, density) and examine the direct influence of flow submergence on particle

motion. Although several researchers in the past have studied the effects of flow submergence (e.g. Hu & Hui, 1996; Lajeunesse et al., 2010; Lee & Hsu, 1994; Niño & Garcia, 1998), their experiments were performed under conditions when the change in flow submergence was accompanied with changes in either shear velocity u_*, Shields parameter $\tau*$ or particle diameter D. Similarly, there is a need for a direct assessment of the effect of the particle density ρ_p with all other controlling parameters kept constant.

This paper attempts to provide a better quantification of the role of flow submergence and particle density in saltating motion by explicitly studying their effects in isolation from other factors, i.e. keeping other controlling parameters (e.g. u_*, D) constant. We first outline our methodology (section 2) and introduce a new technique for determining the duration and height of particle flights using the impact data from the records of instantaneous pressure acting on multiple bed particles (section 3). The proposed approach complements the previously used high-speed photographic/video techniques coupled with image analysis (e.g. Ancey et al., 2002; Campagnol et al., 2013; Drake, Shreve, Dietrich, Whiting, & Leopold, 1988; Hergault et al., 2010; Keshavarzy & Ball, 1999; Radice, Malavasi, & Ballio, 2006; Schuyler & Papanicolaou, 2000). Then, we report the saltation parameters, covering wider ranges of the flow submergence and particle density than have been explored to date (sections 4 and 5).

The work presented in this paper is part of a larger research programme focused on the mechanisms of particle entrainment and motion. In this paper, we use the pressure data to determine only the flight durations and heights of the saltating particles while the comprehensive analysis of differential pressure acting on multiple bed particles is the subject of another publication (Amir, Nikora, & Stewart, 2014).

2 Methodology

Experiments were conducted in a rough-bed open-channel flow with a bed made of spherical glass particles. An array of differential pressure sensors was employed to detect saltating particle impacts with the bed; these were used to determine the flight durations and maximum heights of the saltating particles. To validate the results of this new technique, the motion of the particles was tracked and their trajectories were determined using a particle image velocimetry (PIV) system. A standard experiment included synchronous measurements of pressure at multiple locations on the bed, water and particle motion using PIV, and water surface elevation. Each experiment was repeated under a number of hydraulic conditions which are described in the following sections.

2.1 *Facility, set-up, and instrumentation*

Experiments were carried out in the Aberdeen Open Channel Facility (AOCF). The AOCF is comprised of three main

components: an open channel flume, an instrumental carriage and an advanced modular PIV system. The re-circulatory flume is equipped with two pumps and has a working length of 18 m and is 1.18 m wide. The entrance to the flume contained a combination of honeycomb mesh and steel vanes aimed at straightening and conditioning the entrance flow. Backwater profiles were controlled by a weir consisting of 12 vertical vanes. An instrumental carriage ran along the length of the flume on rails attached to the top of the side walls and carried instrumentation for measuring bed and water surface elevations, data logging equipment and a PIV system (computers, laser, optics). Flow rate was measured using an electromagnetic flow meter located in the discharge pipe prior to the entrance of the flume. Three ultrasonic range finders (URFs), two Baumer (UNAM 12U9914/S14, Swindon, UK) and one Banner (U-GAGES18U, Wickford, UK), were used for bed and water surface profiling (e.g. to check and ensure uniform flow conditions). The measured bed slope was accurate to within $\pm 1.4\%$ while the flow meter was accurate to within $\pm 0.5\%$ of the measured flow rate. Uncertainty in the flow depth (estimated by comparing ultrasonic measurements with PIV images) was ± 0.3 mm.

The bed used in this study comprised one layer of fixed spheres in a hexagonally close packed pattern, which covered the whole flume bed. The spheres were made of transparent glass and were 16 mm in diameter with a tolerance of ± 0.25 mm. Perforated stainless steel plates (2 mm thick), which were screwed to the bed, held the spheres in place and ensured highly regular hexagonal packing along the length of the flume. Black glass marbles with a finer tolerance of ± 0.127 mm replaced the transparent spheres within the PIV measurement area (12.6 m from the flume entrance) in order to minimize laser light scattering. Two types of spherical particles were chosen in this study for saltation experiments. Type 1 was made of Delrin, with a density of 1.38 g cm^{-3}, whereas type 2 was made of Nylon, with a density of 1.12 g cm^{-3}. Both particle types had a diameter of 16 ± 0.025 mm and were placed on a bar beneath them to protrude above the surrounding fixed glass spheres at a desired elevation (Fig. 1).

Point measurements of differential pressure on the flume bed were made using Honeywell Piezo resistive sensors (24PCE series, Honeywell, Morris Plains, NJ, USA). The sensors had a full scale range of 3450 Pa. Each pressure sensor had a high pressure port (voltage increases with increasing pressure) and a low pressure port (voltage decreases with increasing pressure). The diameters of the high and low pressure ports were 1 mm and 1.5 mm and their depths were 8 mm and 6.5 mm, respectively. In order for the sensors to be discretely incorporated within the bed roughness they had to first undergo some modification. More specifically, the cylindrical pressure ports were machined down and following this they were fitted inside two hollow plastic hemispheres, representing an instrumented particle. The instrumented particles were then configured in one of two orientations. In the first orientation, the pressure ports were aligned with the flow in order to measure pressure fluctuations
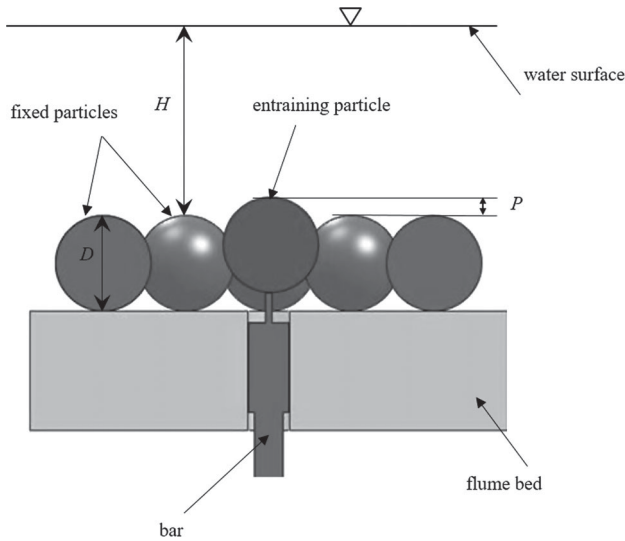
Figure 1 Entraining particle support mechanism and parameter definitions

representing the drag force. In the second orientation, the ports were aligned perpendicular to the bed to measure pressure fluctuations representing the lift force. A total of 23 pressure sensors were simultaneously used in this study, 16 of these were drag sensors and seven were lift sensors. Their arrangement is shown in Fig. 2.

The section covered by the pressure sensors was 275 mm long (in the *x*-direction) and 192 mm wide (in the *y*-direction). The spacing between the drag sensors was 27.7 mm in the *x*-direction and 32 mm in the *y*-direction. The centre of the measurement section is indicated by position #1 in Fig. 2 where

particles were placed to undertake saltation experiments. In order to minimize the effects of forces acting on the surrounding spheres during the entrainment experiments, the six spheres (solid black in Fig. 2) were glued to each other around the entraining particle. The same ring of spheres was used throughout the course of this study. The pressure sensors were connected to National Instruments (NI, Austin, TX, USA) 9237 C Series I/O modules and the measurements were made at a sampling frequency of 10 kHz (with a view of data subsampling), synchronously with PIV and water level recordings.

The Aberdeen PIV system used in this study has been developed in house at the University of Aberdeen by Dr Stuart Cameron (Cameron, 2011; Cameron et al., 2013). The system comprises four cameras (DALSA 4M60, CMOS sensor, Waterloo, Canada, 2352 × 1728 pixels resolution at 62 frames per second) with adjustable Scheimpflug mounts which allow non-orthogonal viewing of the light sheet plane. Laser light is provided by twin Nd:YAG lasers (Oxford Lasers Neo 50-100/100-50 PIV, Didcot, UK) set to operate in a pulsed mode. The PIV sampling frequencies for velocity measurements (32, 50 or 100 Hz) varied depending on the flow submergence, with the lowest frequency associated with the deepest flow. The same PIV system was used to track the motion of the entrained particles. The camera frequency was reduced with increasing submergence so a larger field of view could be captured. The cameras therefore operated at 200, 100 and 64 frames per second for scenarios 1, 2 and 3, respectively (see section 2.2 and Table 1). This allowed us to track particle position from frame to frame, with time resolution varying between 0.01 to 0.03 s depending on the flow submergence. A technique similar to
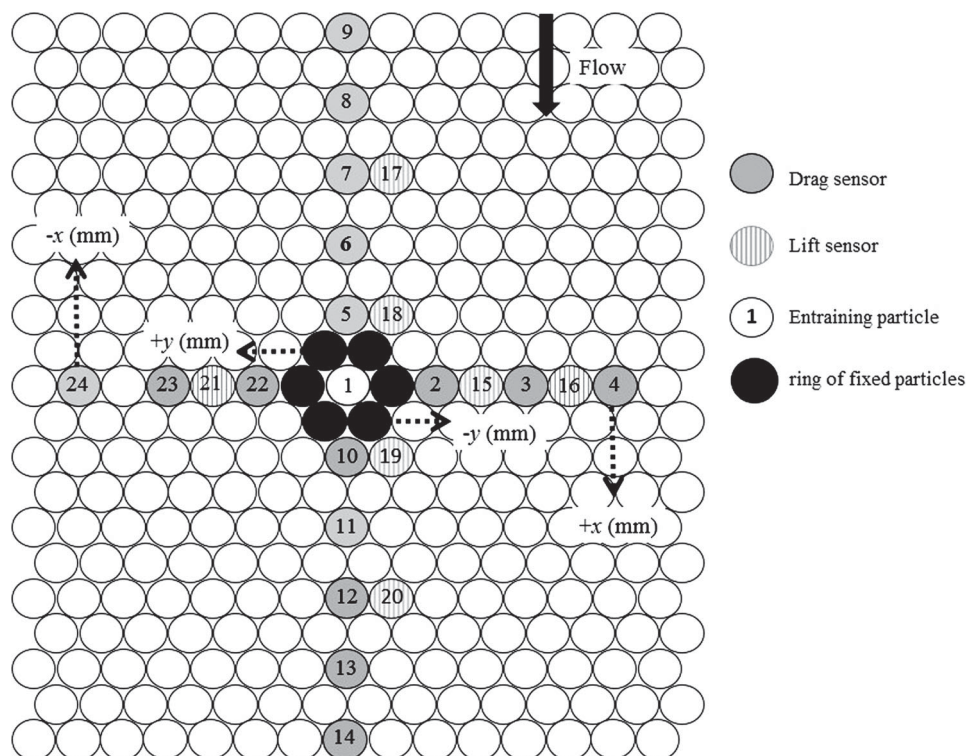

Figure 2 Arrangement of bed particles instrumented with differential pressure sensors

Table 1   Flow configurations

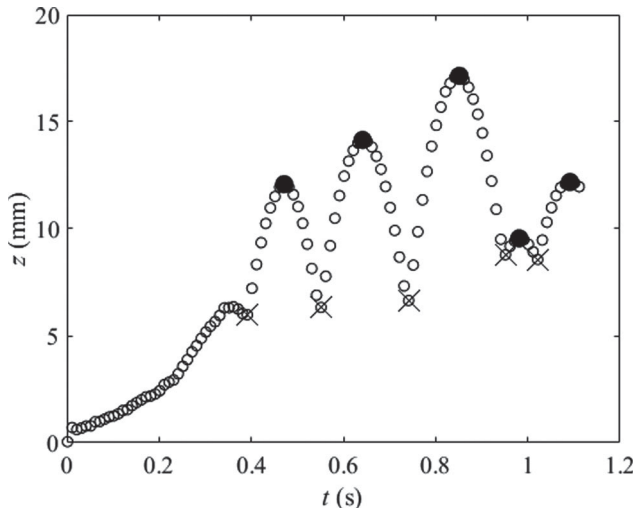| Scenario #	ρ_p/ρ_f	P/D	S_b	Q (m³ s⁻¹)	H (mm)	U_b (m s⁻¹)	τ_*	B/H	H/D	F	R$_*$	R$_b$
1	1.12	0.16	0.006	0.0136	30	0.385	0.094	39.3	1.9	0.71	1260	11545
1	1.38	0.483	0.006	0.0136	30	0.385	0.030	39.3	1.9	0.71	1260	11545
2	1.12	0.117	0.00257	0.0382	70	0.462	0.094	16.9	4.4	0.56	2940	32364
2	1.38	0.417	0.00257	0.0382	70	0.462	0.030	16.9	4.4	0.56	2940	32364
3	1.12	0.098	0.0015	0.0728	120	0.514	0.094	9.8	7.5	0.47	5040	61678
3	1.38	0.391	0.0015	0.0728	120	0.514	0.030	9.8	7.5	0.47	5040	61678

Figure 3   Vertical position z of the moving particle plotted as a function of time for run 3. Parameters are $\rho_p/\rho_f = 1.38$, $P/D = 0.391$ and $H/D = 7.5$ (Table 1, Fig. 1). The origin $z = 0$ is at the centre of a particle before its entrainment

2.2 *Experimental scenarios and procedure*

A total of three flow scenarios were tested as summarized in Table 1. In the table, ρ_p/ρ_f is the ratio of an experimental particle density to fluid density; P/D is the ratio of the particle protrusion P (measured from the top of the surrounding fixed particle to the top of the experimental particle before entrainment as shown in Fig. 1) to particle diameter D; S_b is bed slope; H denotes the flow depth (measured from the particle tops to the water surface, Fig. 1); $U_b = Q/A$ is the bulk mean velocity (where Q is the flow rate and A is the cross sectional area of the flow); R$_b = (U_bH)/\nu$ is the bulk Reynolds number (where ν is the fluid kinematic viscosity); F $= U_b/(gH)^{0.5}$ is the Froude number; B/H is the aspect ratio (where B is the flume width); H/D is the flow submergence; u_* is the shear velocity, estimated in this study as $u_* = (\tau_b/\rho_f)^{0.5} = (gHS_b)^{0.5} = 0.042$ m s⁻¹; τ_b is bed shear stress; and R$_* = (u_*H)/\nu$ is the friction Reynolds number. The shear velocity $u_* = 0.042$ m s⁻¹ was kept constant as well as the particle Reynolds number R$_p = Du_*/\nu$ that had the same value of 672 for all three studied flows. Although u_* was kept constant throughout the course of this study, the Shields number $\tau_* = (\rho_f gHS)/[(\rho_p-\rho_f)gD]$ varied as it involves the particle density (Table 1). Also, Table 1 shows that the P/D values were reduced with increasing H/D. This is because as the flow submergence increases (and so does the flow speed), the particle becomes more prone to entrainment. Therefore, in order to retain an average entrainment time of 2min, P/D was reduced at higher flow submergences.

It can be seen that all studied flows were fully turbulent with the bulk Reynolds number varying from 11,545 to a maximum of 61,678. Further, all flows were in the subcritical regime, with the Froude number ranging between 0.47 and 0.71. All flows are considered of low to intermediate submergence with $H/D \leq 7.5$ (as per classification of Nikora et al., 2007). The value of R$_p$ well exceeds the threshold of ∼ 70 to achieve fully rough-bed conditions. Given the high aspect ratios ($B/H \geq 10$), two-dimensional flow conditions are expected along the channel centreline according to empirical guidelines available in the literature (e.g. Nezu & Nakagawa, 1993). The measurement section was located at a minimum of 100H (for $H = 120$ mm) from the leading edge of the roughness transition at the flume entrance, and thus the flow in the measurement region can be assumed to be fully developed (this was quantitatively verified in Stewart, 2014). Water surface profiles were measured using

the intensity-gradient-based Canny edge detector (Canny, 1986) was used to track the position of the particle; this required the particle to be simultaneously tracked in two different camera images, and the mapping of the camera images into real space. The tracking ran from the start of the experiment recording until the particle could no longer be seen by both cameras. From the point of entrainment the tracking was then manually checked and edited as required to improve the accuracy. Stereoscopic reconstruction was performed on the coordinates of the particle centre from the perspective of two independent cameras to give the location of the particle in three-dimensional space at each point in time. The spatial resolution was such that the particle diameter was about 160 pixels and the size of the field of view of the order of 31 × 1.9, 31 × 4.4 and 31 × 7.5 particle diameters for scenarios 1, 2 and 3, respectively (Table 1).

With these conditions, we were able to determine the position of the particle centre on an image with a precision of 0.032 mm. A sub-pixel resolution algorithm was used to enhance the resolution of images. This method is based on the analysis of multi-images which are fast recorded during the fine relative motion of image and pixel arrays of CCDs. More details can be found in Witz (2014). An example of a time series of the vertical particle position z obtained with this approach is shown in Fig. 3. The origin $z = 0$ is at the centre of a particle before its entrainment.

the URFs to verify that the flow remained uniform along the length of the channel.

The influence of the particle density and flow submergence on particle saltation was investigated by performing six series of experiments consisting of three flow scenarios as shown in Table 1. For each flow scenario, two series of saltation experiments were conducted using different entraining particles (i.e. $\rho_p/\rho_f = 1.12$ and 1.38). Saltation experiments began by setting the flow rate, bed slope, flow depth, and particle protrusion required to entrain each type of protruding particles. A particle replacement device was designed which allowed the entraining particles to fall under gravity into its required position. With the desired uniform flow conditions achieved, particle protrusion was set so that entrainment could occur approximately once every 2 min. This was needed to allow any transient effects associated with the particle replacement device to dissipate. The PIV system was aligned with the flume centreline and the centre of the protruding particle to capture the streamwise vertical plane. This was left running until the particle was entrained by the flow. The PIV measurements were continuously made but only the 30 s records were retained for the follow-up analysis (20 s prior to entrainment and 10 s after entrainment). For each particle and protrusion combination, 25 entrainment experiments were carried out to achieve sufficient statistics for particle trajectories.

3 Measurement of particle motion parameters using instantaneous pressure data: a new technique

3.1 *Pressure-based measurement technique*

It was anticipated that the arrangement of pressure sensors would cover a wide area of the measurement section to allow the investigation of temporal and spatial correlations between

drag–drag, drag–lift and lift–lift pressure sensors. While this investigation has been reported in Amir et al. (2014), the employed set-up of the pressure sensors can also be used to estimate the durations and heights of particle flights (i.e. between two successive collisions with the bed). After the particle has been entrained, each impact with the bed generates a pressure impulse in the output signal of the pressure sensors. If t_i is the time moment at which the pressure impulse is generated then the flight duration τ can be calculated as $\tau = t_i - t_{i-1}$. The peak-to-trough amplitude of the pressure impulse gives an indication of how high the particle travels in the wall-normal direction following its impact with the bed. Here, peak-to-trough amplitude is the change between peak (highest value) and trough (lowest value which can be negative), as shown in Fig. 4. The maximum height of the particle after each impact with the bed can either be related to the peak-to-trough amplitude of the preceding impulse or the following impulse in the pressure signal. Our tests have shown that the maximum height of the particle is stronger correlated with the peak-to-trough amplitude of the preceding impulse. These tests are described in the following section. From here onwards, we will refer to this new technique as "pressure sensors method".

3.2 *Validation with PIV tracking method*

An example of trajectory of the moving particle from PIV tracking shown in Fig. 3 is representative of observations of the bedload particles exhibiting continuous periods of motion, called flights. The points marked with symbols " × " and "•" in Fig. 3 represent the times at which the particle comes into contact with the bed and the maximum vertical height reached following an impact, respectively (Witz, 2014). The different z values when the particle comes into contact with the bed result
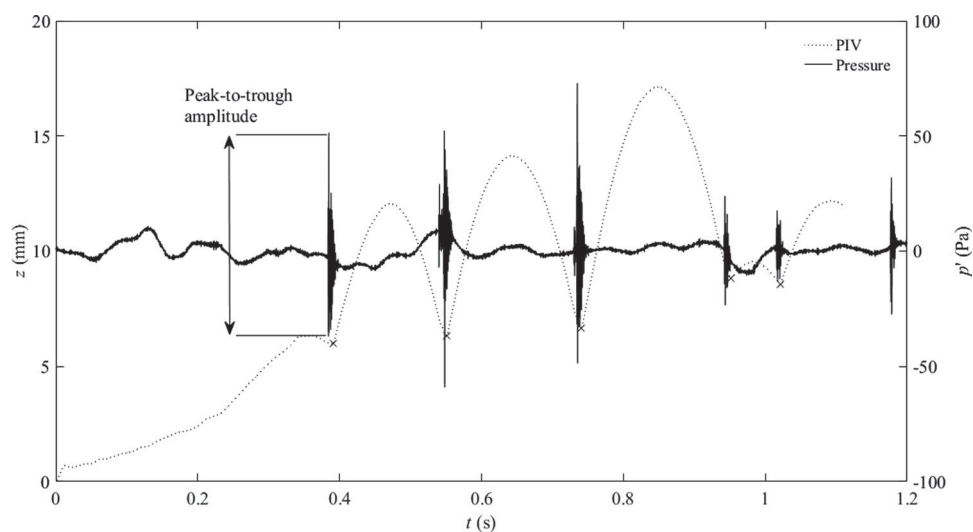

Figure 4 Instantaneous pressure fluctuations (sensor #9, Fig. 2) plotted as a function of time with vertical position z of the moving particle from PIV superimposed for run 3. Parameters are $\rho_p/\rho_f = 1.38$, *P/D* = 0.391 and *H/D* = 7.5 (Table 1, Fig. 1). Note that slight time shifts of a pressure peak in relation to a PIV recorded collision, occasionally observed, reflects "imperfect" synchronization between PIV frames and pressure sensors

from the fact that the particle hits a different point along the surface of the fixed spheres. If the particle hits the top of a fixed sphere, the highest value of z is registered.

The definitions for estimation of particle impact times and particle heights using pressure data are shown in Fig. 4, where instantaneous pressure fluctuations are plotted as a function of time. The particle trajectory obtained using PIV is superimposed in Fig. 4 with pressure data to make a direct comparison between the two methods. It can be seen that at the point at which the particle impacts the bed, an impulse is generated in the pressure signal which coincides with the points marked with symbol × in Fig. 4. There is a good agreement between locations of the impulse in the pressure signal and the impact points. Figure 4 also shows that the peak-to-trough amplitude of the pressure impulse is proportional to the maximum particle height following its impact with the bed. Indeed, Fig. 4 demonstrates that the gradual increase in the maximum particle height during the first three jumps is reflected in a gradual increase in the peak-to-trough pressure amplitudes. During the fourth jump, the particle loses momentum which results in a much smaller maximum vertical displacement. This observation agrees well with the peak-to-trough amplitude of the preceding pressure impulse which also reduces drastically. It is encouraging to see that although using the PIV method the particle cannot be tracked anymore once it leaves the tracking window, the pressure sensors may still provide useful information on particle flight durations and heights. This is evident in Fig. 4 where an additional particle impact is detected in the pressure signal while the PIV method fails to track the particle for $t > 1.1$ s. For an illustration purpose, Fig. 4 only covers the time up to 1.2 s, but our data have shown that the particle impacts can be picked up by the pressure sensors at least up to 2.5 s after entrainment. This would result in estimating at least twice as many flight durations and heights of the particle for each experiment using the "pressure sensors method". Here, the signal from pressure sensor #9 (Fig. 2) was used in Fig. 4 as an example. The signals from all the other sensors produced peaks at the same times without any time delay, therefore producing the same results. Figure 4 illustrates that the pressure sensors method indicates flight durations and heights reasonably well for one selected experiment. It is however important to validate these results against the PIV method for all three runs that were conducted in this study.

Figure 5a shows the particle impact time moments t_i, obtained from pressure sensor #9 (Fig. 2), plotted against values obtained using the PIV tracking method, $t_{i(PIV)}$. An excellent collapse onto the line of equal values is evident for all flow submergences. Figure 5b shows the particle flight durations obtained using pressure sensors, $\tau = t_i - t_{i-1}$, against $\tau_{(PIV)}$ from the PIV tracking method. The data points collapse around a line of equal values reasonably well. Similar results were also observed for the lighter saltating particles (i.e. for particles with $\rho_p/\rho_f = 1.12$) at all flow submergences (not shown here). It is also worth noting that the output signals from all pressure
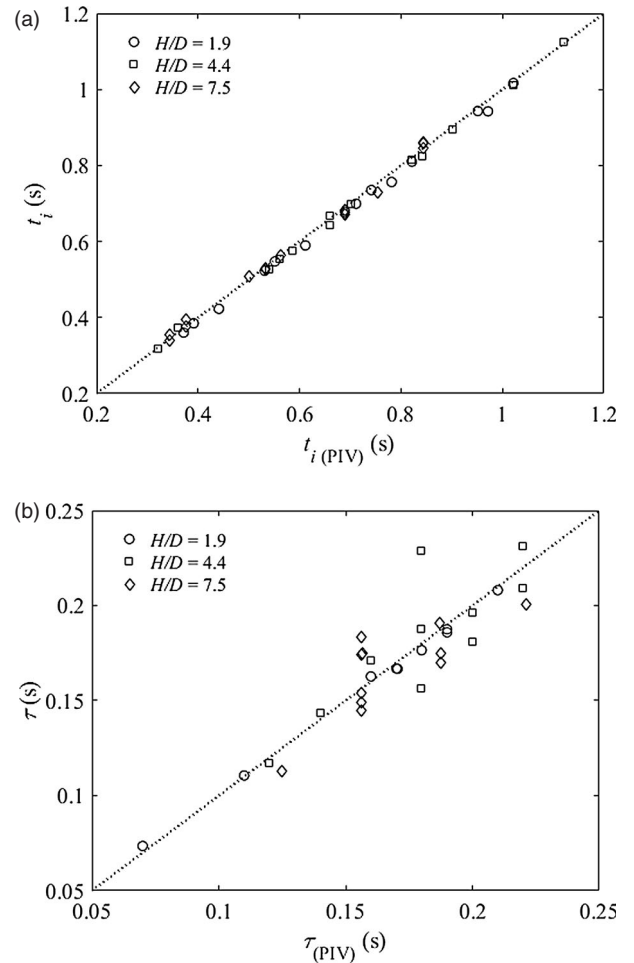

Figure 5   Particle impact times (a) and flight durations (b), obtained from pressure sensor #9, against the data from PIV tracking for a particle with $\rho_p/\rho_f = 1.38$. Dashed lines are lines of equal values ($y = x$)

sensors provided the same result. The mean relative errors in the estimations of impact times and flight durations τ were 0.8% and 6.1%, respectively (if PIV tracking is assumed to provide true values).

Figure 6 shows the plot of peak-to-trough amplitude a of the preceding peak in the pressure signal against the following maximum particle height z_m obtained using the PIV-based tracking method. The data points reasonably collapse onto the linear fit line $z_m = ka$, with the mean relative error in the estimates of flight heights z_m as 27.2% (if PIV tracking is assumed to provide true values). A fair scatter of the data points in Fig. 6 is due to two key reasons. First, the amplitude of the pressure impulse depends on the exact location at which the moving particle hits the fixed spheres. For instance, if the particle lands right on top of the resting sphere, it will generate amplitude different from that when it lands in between the resting spheres. If the mobile particle was to land at exactly the same location on a bed particle every time it came into contact with the bed, we would have had a better correlation. Second, the pressure amplitude due to the
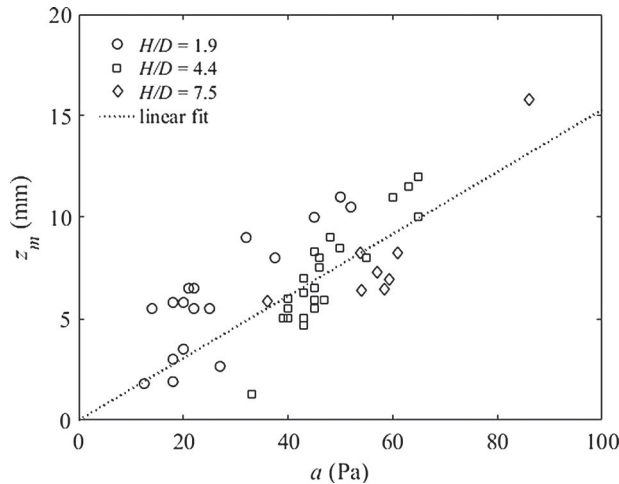
Figure 6   Peak-to-trough amplitude of the pressure impulse against maximum particle height from PIV tracking for a particle with $\rho_p/\rho_f = 1.38$. Dashed line is the linear fit of the data, $z_m = 0.155a$. The output signal from pressure sensor #9 is used

collisions is superimposed with the effects of turbulent coherent structures which themselves are random.

Unlike for the particle impact times, where every sensor in the measurement section produced a pressure peak at the same time, the output signal from the pressure sensors revealed that the peak-to-trough amplitude at each impact varied from one sensor to another, reflecting local set-ups and individual sensitivity. Hence, the dimensional factor k in $z_m = ka$ is sensor-dependent. The sensors located upstream of the entraining particle provided a better correlation with the particle height than the downstream sensors. Out of all the sensors located upstream of the entraining particle, sensor #9 correlated the most with the particle height and therefore the data from this sensor was used in Fig. 6. From here on, the peak-to-trough amplitude from pressure sensor #9 will be used as a surrogate for the particle flight height throughout the analysis. Our data also revealed that the dimensional factor k in $z_m = ka$ depends on the particle density, being approximately two times higher for lighter particles (i.e. $\rho_p/\rho_f = 1.12$).

Although the relative errors for flight heights are appreciably higher compared to 6.1% for flight durations, these errors are random and non-correlated allowing computation of unbiased bulk statistics, at least for odd moments. Also, due to linearity of $z_m = f(a)$ the appropriately normalized statistical measures (e.g. skewness coefficient) are identical for z_m and a.

3.3   *Advantages of the pressure sensors method*

We have shown above that the pressure sensors can be used to estimate flight durations with fairly good accuracy and to estimate maximum flight heights of moving particles with reasonable accuracy, especially in relation to the bulk statistics. The main advantage is that it is not necessary for a particle to be in direct contact with the pressure sensor for it to detect a collision. The PIV method relies on a measurement window size, which in the present study allowed tracking the particles in the streamwise direction for no more than 200 mm. With this restriction, only one to five particle impacts with the bed could be recorded on average per experiment. On the other hand, pressure sensors allowed us to record as many as twice the number of particle impacts per experiment. By appropriately spacing successive pressure sensors along the bed, one could cover the entire length of the downstream (of the entraining particle) part of the flume and therefore record essentially unlimited numbers of particle impacts on the bed. Thus, our results suggest that the use of the pressure sensors can be a simple and affordable way of collecting massive data on particle motion. This can prove very useful for obtaining large datasets for statistical analysis.

Recently, researchers have used passive acoustic instruments, such as hydrophones and geophones, for the measurement of the bedload rate in water flows (Rickenmann, Turowski, Fritschi, Klaiber, & Ludwig, 2012; Thorne, 2014; Tsakiris, Papanicolaou, & Lauth, 2014; Turowski & Rickenmann, 2009). Their work focused on en masse sediment movement whereas our technique provides an alternative method for studying individual particle motion, thus complementing the acoustic techniques.

4   Statistics of particle flight durations and amplitudes

4.1   *Probability density functions (PDF) of particle flight durations and amplitudes*

The PDFs of particle flight durations normalized by u_*/D are shown in Fig. 7. The vertical lines represent the mean values of flight duration for each PDF. The normalization on u_*/D is selected as $\tau u_*/D \sim L/D$, where L is the particle flight length (i.e. distance between two successive collisions). Figure 7a illustrates that for $\rho_p/\rho_f = 1.12$, the PDFs at $H/D = 1.9$ and 7.5 reveal well-defined peaks corresponding to the most probable (mode) flight durations. It can also be seen that the mean values at $H/D = 1.9$ and 7.5 are both close to their mode values. However, for $H/D = 4.4$, the peak of the PDF is much less defined but its mean value (indicated by a vertical dashed line) is still fairly close to the mode value. The vertical lines also show that the mean value of the flight duration increases with flow submergence, indicating that particle impacts with the bed become less frequent at higher H/D. For $\rho_p/\rho_f = 1.38$, Fig. 7b shows that all three PDFs reveal well-defined peaks and the mean values coincide with the mode values for each flow submergence. The mean value of the flight duration increases when H/D is increased from 1.9 to 4.4, but further increase in H/D does not increase the mean value (Fig. 7b). Both sets of PDFs in Fig. 7 show that the particle flight duration decreases with increase in particle density. This reflects the fact that lighter particles (with $\rho_p/\rho_f = 1.12$) remain in flight for longer
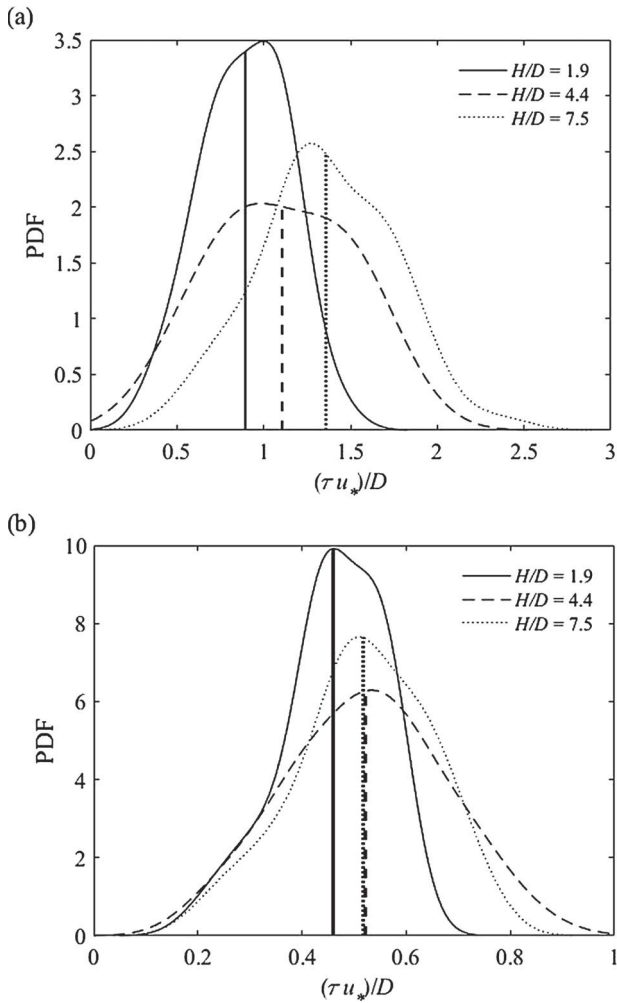
(a)

(b)

Figure 7   PDFs of flight durations normalized by u^*/D for particles with $\rho_p/\rho_f = 1.12$ (a) and $\rho_p/\rho_f = 1.38$ (b). Vertical lines represent the mean values for each flow submergence

(a)

(b)

Figure 8   PDFs of peak-to-trough pressure amplitude normalized by τ_b for particles with $\rho_p/\rho_f = 1.12$ (a) and $\rho_p/\rho_f = 1.38$ (b). Vertical lines represent the mean values for each flow submergence

periods of time following an impact with the bed than heavier particles (with $\rho_p/\rho_f = 1.38$). Note that due to a reduced number of impacts with the bed, the PDF estimate in Fig. 7a for $H/D = 7.5$ and $\rho_p/\rho_f = 1.12$ was not sufficiently converged. In contrast, approximately twice as many data points were used to construct the PDF at the same H/D for the heavier particles, which resulted in a well-defined peak in Fig. 7b. For the lighter particles, the PDFs are approximately symmetrical for all H/D as shown in Fig. 7a. For the heavier particles, Fig. 7b shows that while the PDFs for $H/D = 4.4$ and 7.5 are approximately symmetrical, the PDF for $H/D = 1.9$ is clearly negatively skewed.

The PDFs of particle peak-to-trough pressure amplitude normalized by the bed shear stress τ_b are shown in Fig. 8. We use here the directly measured amplitudes which can be converted to actual flight heights using linear best-fit equations as described in section 2.2 and illustrated in Fig. 6. For $\rho_p/\rho_f = 1.12$ (Fig. 8a), the PDFs exhibit well-defined peaks for all flow submergences. It can be seen that the PDFs are not symmetric but are instead positively skewed so that their respective mean values
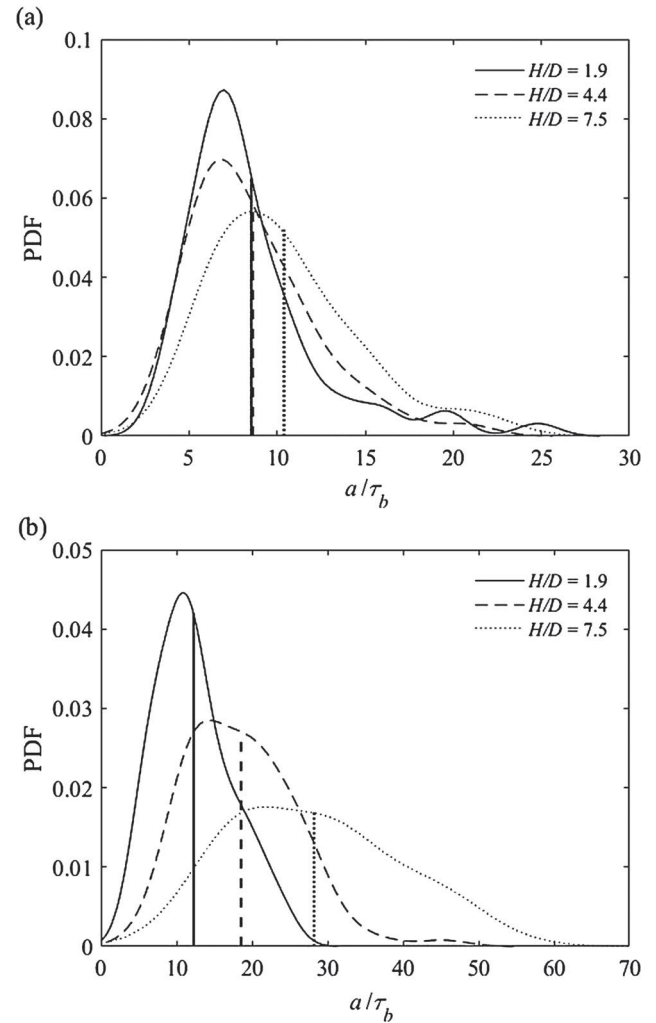
are larger than their mode values. Figure 8a shows that for lighter particles, the normalized mean value of the amplitude remains unchanged when H/D is increased from 1.9 to 4.4. However, further increase in H/D causes the mean amplitude to rise as well. Similar trends are also seen for the heavier particles in Fig. 8b which shows that the mean normalized value of a increases with H/D as indicated by the vertical lines. Here flow submergence effects are evident even for lower H/D. Figure 8 also demonstrates that the peak-to-trough amplitudes of the heavier particles are higher than those for the lighter particles for all H/D. Indeed, the normalized mean values of a for the heavier particles are approximately 1.5–2.5 times higher than for the lighter particles. The heavier particles have a greater impact with the bed and therefore generate higher values of a in the pressure signal; this effect gets more significant at higher H/D. If we take into account the fact that the dimensional factor k in $z_m = ka$ depends on the particle density (section 3.2), then our data suggest that on average the lighter particles fly higher, although pressure amplitudes for lighter particles in Fig. 8 is lower (Witz, 2014).

4.2 Statistical moments

We now examine the bulk statistics of τ and a, including the mean μ_x, standard deviation σ_x, skewness $S_x = [(x-\mu_x,)^3]/\sigma_x^3$, and kurtosis $K_x = [(x-\mu_x,)^4]/\sigma_x^4 - 3$, where x stands for τ or a and square brackets mean the mathematical expectation. The mean values of the particle flight duration μ_τ normalized by u_*/D are plotted as a function of H/D in Fig. 9a. The results show that for $\rho_p/\rho_f = 1.12$, the mean value increases fairly linearly with H/D, whereas for $\rho_p/\rho_f = 1.38$ the mean value remains unaffected at higher H/D. A small increase in μ_τ is however also observed for $\rho_p/\rho_f = 1.38$ when H/D increases from 1.9 to 4.4. These observations reflect the already described features of PDFs in section 3.1.

The standard deviations of the particle flight duration σ_τ normalized by u_*/D are shown in Fig. 9b. For both the lighter and heavier particles, σ_τ increases as H/D is increased from 1.9 to 4.4 but remains unaffected with further increase in H/D. In fact, a small reduction in σ_τ is observed when H/D is increased
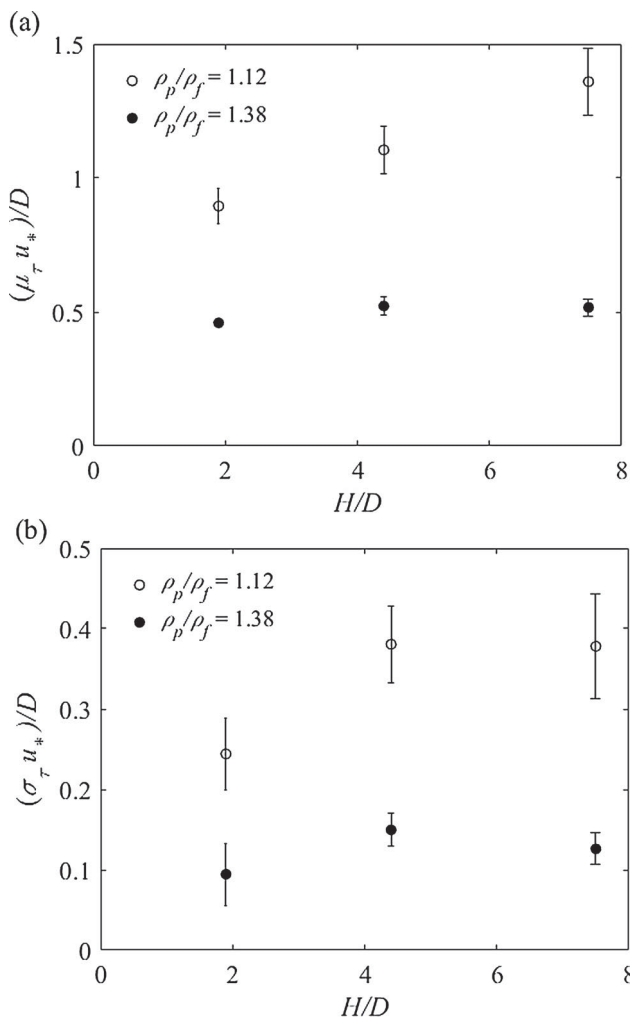

Figure 9   Plots of mean (a) and standard deviation (b) of particle flight durations as a function of flow submergence. The 95% confidence intervals (vertical segments) were estimated using the moving block bootstrap technique as outlined in Garcia, Jackson, and Garcia (2006)

to 7.5 for both particle types (Fig. 9b). The standard deviations are about 27–34% and 20–28% of the mean values for $\rho_p/\rho_f = 1.12$ and $\rho_p/\rho_f = 1.38$, respectively. The skewness S_τ of flight durations for $\rho_p/\rho_f = 1.12$ is close to zero, indicating that their PDFs are fairly symmetric, as could be expected from Fig. 7a. However, for $\rho_p/\rho_f = 1.38$ at $H/D = 1.9$, the skewness S_τ is negative (-0.7), demonstrating that the PDF is not symmetrical and is skewed toward short flight durations as previously suggested by Fig. 7b. At $H/D = 7.5$, the S_τ is also negative (-0.3) but its magnitude is much less than it is for $H/D = 1.9$. However, at intermediate $H/D = 4.4$, the S_τ value is nearly zero for both the heavier and lighter particles. A general trend, therefore, shows that as particles become heavier, the PDFs of their flight durations become more asymmetric.

The kurtosis coefficient K_τ assumes negative values (-0.04 to -1.2) for all experimental scenarios, indicating that the particle flight durations have a flatter distribution for all cases compared to a normal distribution (a value of 3 is subtracted from the normalized fourth moment so that the kurtosis K_τ for the standard normal distribution is zero). The results show that when H/D is increased from 1.9 to 4.4, the values of K_τ become more negative for both the lighter and heavier particles. Further increase in H/D shows no effect in K_τ for the heavier particles, although for the lighter particles K_τ become closer to zero. As indicated by their higher negative values of K_τ, the flight duration distributions for the lighter particles are flatter than for the heavier particles for low and intermediate values of H/D only. In this study, a minimum of about 120 (for lighter particles) and 200 (for heavier particles) impacts were recorded for each flow scenario and thus the sample sizes may not be sufficient to obtain well converged higher order statistics. Therefore, the described trends in the data for higher-order moments should be treated cautiously.

The mean values μ_a of the pressure amplitude normalized by τ_b are plotted as a function of H/D in Fig. 10a. For the lighter particles, the mean values remain mostly unaffected by the changes in H/D, whereas for the heavier particles the mean value increases fairly linearly with H/D. Also, the mean amplitude for each H/D is higher for the heavier particles than for the lighter particles (the reason is explained at the end of section 4.1). Similar trends are also observed for the normalized value of the standard deviation σ_a of the amplitudes (Fig. 10b). While σ_a remains unaffected with varying H/D for the lighter particles, the heavier particles exhibit a linear increase in σ_a with H/D. The standard deviations of a are about 39–47% and 37–41% of the mean values for $\rho_p/\rho_f = 1.12$ and $\rho_p/\rho_f = 1.38$, respectively. The positive values of the skewness S_a (0.4 to 1.8) indicate that the distributions are skewed toward higher amplitudes. Also, the distributions are more skewed for the lighter particles as shown by higher values of S_a. With increasing H/D, the distributions of a tend to become more symmetrical as the values of S_a tend to reduce towards zero value. The kurtosis K_a of the amplitude changes in the range of 3.9 to -0.8 and reveals the following trends. The K_a values become
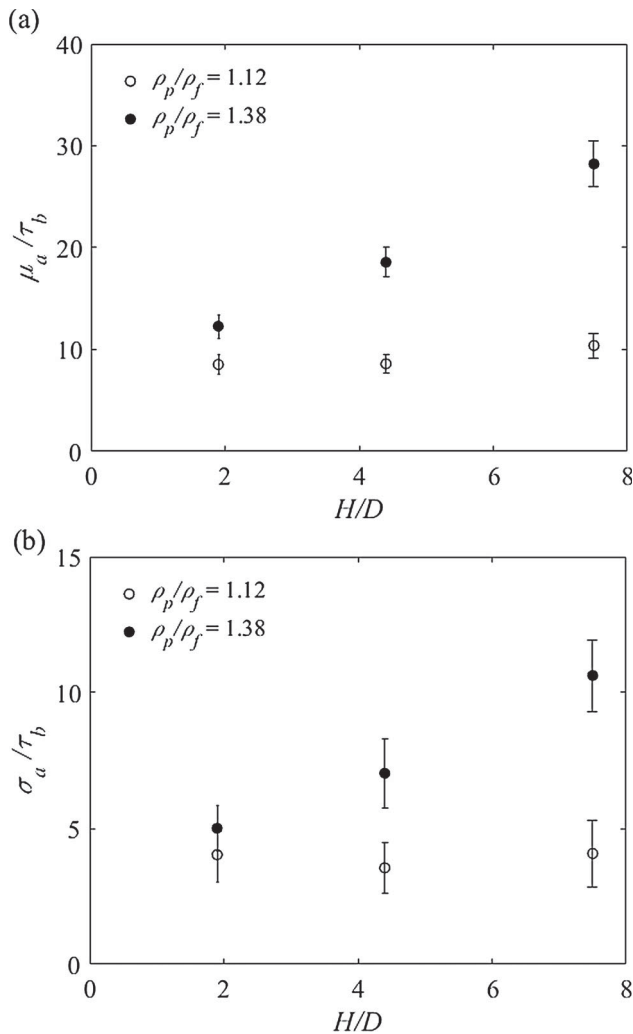
(a)

(b)

Figure 10   Plots of mean (a) and standard deviation (b) of particle flight amplitudes as a function of flow submergence. The 95% confidence intervals (vertical segments) were estimated using the moving block bootstrap technique as outlined in Garcia et al. (2006)

less positive with increasing H/D and tend to reduce towards the normal distribution value of zero. This indicates that for low H/D, both the heavier and lighter particles exhibit sharper and higher peaks compared to flatter and lower peaks for high H/D as shown by their respective PDFs in Fig. 8. As with S_a, the values of K_a are also higher for the lighter particles for each H/D, although the difference between the two is lower for the kurtosis values. Again, the 95% confidence intervals for both skewness and kurtosis are quite wide and therefore a larger sample size would be required to validate the observed trends.

5   Discussion and conclusions

Video imaging techniques have been successfully used in the past to measure and analyse the particle motions in open-channel flows. Up to now, the majority of studies have been focused on exploring the effects on particle motions of $\tau*$ and D. Our results complement the previous work by explicitly studying the effects of flow submergence and particle density at

constant values of $\tau*$ (or u_*), and D. Measurements were made using a novel technique consisting of an array of piezo-resistive differential pressure sensors located within the particles embedded in the granular bed. To validate the results from this new technique, simultaneous PIV measurements were employed.

Using a pressure impulse in the signal of a sensor located upstream of the entrained and saltating particle, we determined particle flight durations and heights. The time moments at which the pressure impulses appear in the signal are used to determine the flight duration, while the magnitude of the peak-to-trough amplitude of the preceding pressure impulse represents the following maximum height of the moving particle. The results obtained using this technique agreed well with those obtained with the PIV tracking technique. Our tests show relatively weaker correlation between the pressure amplitude and the actual maximum particle height compared to data on flight durations. This is because the amplitude of the pressure signal is also affected by the impact location with the resting spheres. Another factor contributing to de-correlation relates to the effects of large-scale coherent structures randomly distributed in time and space, and superimposed with effects of random collisions.

Using a pressure sensor, on average twice as many particle impacts, compared to PIV tracking, were recorded per experiment using the current set-up. However, by laying the pressure sensors covering the entire downstream (of the entraining particle) section of the flume, unlimited numbers of particle impacts can be recorded, generating data comprehensive enough to obtain very well converged statistics. More importantly, it is not necessary for the particle to have a direct impact with the sensor for the collision to be detected. Although the proposed technique works very well for a single particle entrainment, it may not work equally well for multiple entrainments since the pressure sensor cannot distinguish between different particles. Nevertheless, recording the total number of collisions of all moving particles may still be useful as it opens new avenues for measuring the total bedload due to saltating particles.

The PDFs of normalized flight durations are symmetrical in shape with the exception of a PDF for the lighter particles at $H/D = 1.9$, which is negatively skewed. In comparison, Lajeunesse et al. (2010) found that their PDFs for flight durations were positively skewed so that their mean was slightly larger than the mode value. While their particles exhibited intermittent motion composed of the succession of periods of flights and periods of rest, in the present study the flight is instead bounded by successive collisions with the bed for a particle in continuous motion. The discrepancy between the two sets of results may therefore be because of different flight motions. The PDFs of normalized amplitude are positively skewed for all cases and the results indicate that the maximum vertical height increases with H/D. These results agree well with those published by Abbott and Francis (1977) who also reported that the maximum saltation height of the entraining particle increases with the flow submergence. It is important to mention that the lighter particles for the lowest submergence case interacted with the free
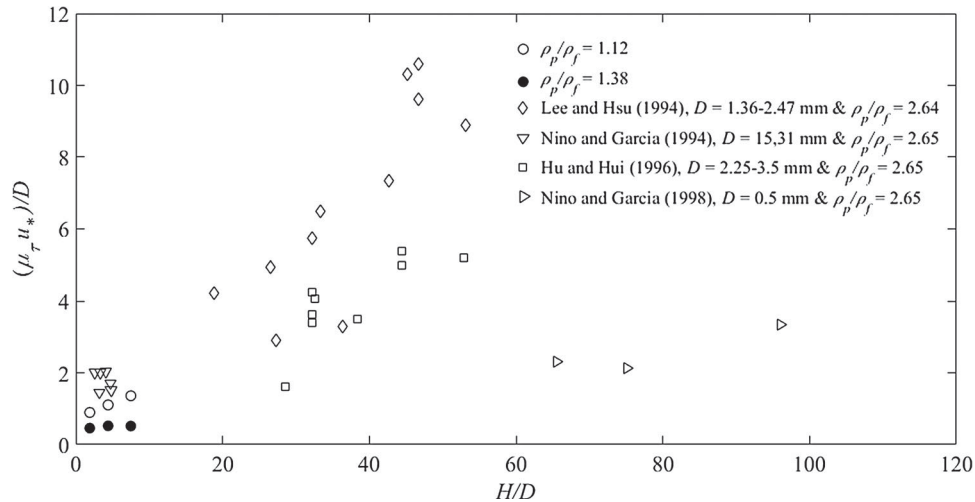
Figure 11 Mean particle flight durations (normalized by u^*/D) as a function of flow submergence. Hollow and filled circles correspond to the present data

surface for some runs. This was observed in the PIV images, whereas such information cannot be obtained if the pressure sensors method is used. Similarly, the lateral movement of the entraining particles can be detected from PIV but the pressure sensors cannot display this information. However, the majority of the particles moved along a straight path with the exception of few, which slightly moved sideways.

The obtained statistics of particle flight durations can be compared to those obtained in previous studies. For example, Lee and Hsu ([1994](#)), Niño and Garcia ([1994](#)), Hu and Hui ([1996](#)), and Niño and Garcia ([1998](#)) obtained values of μ_τ (normalized by u_*/D) which ranged from 2.2 to 10.6, 1.4 to 2.0, 1.6 to 5.3, and 1.49 to 2.45, respectively. These results are plotted in Fig. 11 along with the present data for both lighter and heavier particles. The general trend in Fig. 11 shows that the normalized value of μ_τ increases with increasing H/D for each particular set of measurements. Most of the previous measurements were undertaken for very high values of H/D (owing to smaller particle diameters), apart from the study of Niño and Garcia ([1994](#)), which considered small values of H/D (in the range of 2.6 to 4.7) and used relatively large particles (15 and 31 mm in diameter). It is encouraging to see that our values show a good qualitative agreement with Niño and Garcia's data (1994) (Fig. 11). Note the present measurements not only cover low to intermediate submergences, as in Niño and Garcia ([1994](#)), but also examine the effect of submergence at a constant value of u_*. Both published and present results in Fig. 11 show that apart from H/D, particle flight duration is also dependent on particle sizes and relative densities. The exact nature of these dependencies remains unclear and should motivate the design of future experiments.

Our data related to the flight peak-to-trough amplitude complements the results of Abbott and Francis ([1977](#)), Niño et al. ([1994](#)), Lee and Hsu ([1994](#)), and Niño and Garcia ([1998](#)) obtained for the maximum saltation heights and highlighting their dependence on the dimensionless bed shear stress τ^*. The results from the present experiments show that the amplitude

(and therefore the maximum saltation height) increases with H/D at constant τ^* (or u_*). In addition, Niño and Garcia's ([1998](#)) finding that the standard deviations of the maximum saltation heights were about 30–40% of the mean values agrees well with the corresponding values in our study, i.e. 37 to 47%.

As the methodology of the present study had to be validated first, a fairly low number of scenarios were tested including three flow submergences and two particle densities. It is our intention to expand this investigation so that a wider range of particle densities and flow submergences will be included in our future experiments. It is also important to emphasize that the present results were obtained over a fixed bed with a single particle entrainment. In reality, mean and turbulent flow properties over a mobile bed may differ. However, the available information on potential differences is still limited and relates to fairly narrow ranges of control parameters and/or experimental scenarios. Further work is therefore required for mobile bed cases to develop better understanding of flow modification and the effects it may have on particle flight durations and maximum saltation heights.

Acknowledgements

Notation

a = peak-to-trough amplitude of the pressure impulse (Pa)
B = flume width (m)
D = particle diameter (m)
F = Froude number ($-$)
g = gravity acceleration (m s^{-2})
H = flow submergence (m)
K_a = kurtosis of particle flight peak-to-trough amplitude ($-$)
K_τ = kurtosis of particle flight duration ($-$)
L = particle flight length (m)
P = particle protrusion (m)
Q = flow rate (m^3 s^{-1})
R_* = friction Reynolds number ($-$)
R_b = bulk Reynolds number ($-$)
R_p = particle Reynolds number ($-$)
S_a = skewness of particle flight peak-to-trough amplitude ($-$)
S_b = bed slope ($-$)
S_τ = skewness of particle flight duration ($-$)
t = time after particle entrainment (s)
t_i = particle impact time (s)
u_* = shear velocity (m s^{-1})
U_b = bulk velocity (m s^{-1})
z = vertical height of particle (m)
z_m = maximum vertical height of a particle following an impact (m)
μ_a = mean value of particle flight peak-to-trough amplitude (Pa)
μ_τ = mean value of particle flight duration (s)
ρ_f = density of fluid (kg m^{-3})
ρ_p = density of entraining particle (kg m^{-3})
σ_a = standard deviation of particle flight peak-to-trough amplitude (Pa)
σ_τ = standard deviation of particle flight duration (s)
τ^* = dimensionless critical shear stress (Shields parameter) ($-$)
τ_b = bed shear stress (Pa)
τ = particle flight duration (s)

References

Abbott, J. E., & Francis, J. R. D. (1977). Saltation and suspension trajectories of solid grains in a water stream. *Philosophical Transactions Royal Society London*, *284A*, 443–471.

Amir, M., Nikora, V., & Stewart, M. (2014). Pressure forces on sediment particles in turbulent open-channel flow: A laboratory study. *Journal of Fluid Mechanics*, *757*, 458–497.

Ancey, C., Bigillon, F., Frey, P., Lanier, J., & Ducret, R. (2002). Saltating motion of a bead in a rapid water stream. *Physical Review E*, *66*, 036306–1–16.

Ancey, C., Davison, A. C., Böhm, T., Jodeau, M., & Frey, P. (2008). Entrainment and motion of coarse particles in a shallow water stream down a steep slope. *Journal of Fluid Mechanics*, *595*, 83–114.

Bagnold, R. A. (1977). Bed load transport by natural rivers. *Water Resources Research*, *13*, 303–312.

Bialik, R. J. (2011). Particle-particle collision in Lagrangian modelling of saltating grains. *Journal of Hydraulic Research*, *49*(1), 23–31.

Cameron, S. M. (2011). PIV algorithms for open-channel turbulence research: Accuracy, resolution and limitations. *Journal of Hydro-Environment Research*, *5*(4), 247–262.

Cameron, S. M., Nikora, V. I., Albayrak, I., Miler, O., Stewart, M., & Siniscalchi, F. (2013). Interactions between aquatic plants and turbulent flow: A field study using a stereoscopic PIV system. *Journal of Fluid Mechanics*, *732*, 345–372.

Campagnol, J., Radice, A., Nokes, R., Bulankina, V., Lescova, A., Ballio, F. (2013). Lagrangian analysis of bed-load sediment motion: Database contribution. *Journal of Hydraulic Research*, *51*(5), 589–596.

Canny, J. F. (1986). A computational approach to edge detection. *IEEE Transactions on Pattern Analysis and Machine Intelligence*, *PAMI-8*(6), 679–698.

Cooper, J. R., Aberle, J., Koll, K., & Tait, S. J. (2013). Influence of relative submergence on spatial variance and form-induced stress of gravel-bed flows. *Water Resources Research*, *49*, 5765–5777.

Dey, S. (2014). *Fluvial hydrodynamics. Hydrodynamic and sediment transport phenomena*. Berlin: Springer.

Drake, T. G., Shreve, R. L., Dietrich, W. E., Whiting, P. J., & Leopold, L. B. (1988). Bedload transport of fine gravel observed by motion-picture photography. *Journal of Fluid Mechanics*, *192*, 193–217.

Fernandez-Luque, R., & Van Beek, R. (1976). Erosion and transport of bed-load sediment. *Journal of Hydraulic Research*, *14*(2), 127–144.

Francis, J. R. D. (1973). Experiments on the motion of solitary grains along the bed of a water stream. *Proceedings of the Royal Society A: Mathematical, Physical and Engineering Sciences*, *332*, 443–471.

Garcia, C. M., Jackson, P. R., & Garcia, M. H. (2006). Confidence intervals in the determination of turbulence parameters. *Experiments in Fluids*, *3*, 2410–2420.

Gordon, R., Carmichael, J. B., & Isackson, F. J. (1972). Saltation of plastic balls in a one-dimension flume. *Water Resources Research*, *8*(2), 444–459.

Graf, W. H. (1984). *Hydraulics of sediment transport*. Highlands Ranch, CO: Water Resources.

Hergault, V., Frey, P., Métivier, F., Barat, C., Ducottet, C., Böhm, T., & Ancey, C. (2010). Image processing for the study of bedload transport of two-size spherical particles in a supercritical flow. *Experiments in Fluids*, *49*, 1095–1107.

Hu, C., & Hui, Y. (1996). Bed-load transport. I: mechanical characteristics. *Journal of Hydraulic Engineering*, *122*(5), 245–254.

Hui, Y., & Hu, E. (1991). Saltation characteristics of particle motions in water. *Shuili Xuebo*, *12*, 59–64.

Keshavarzy, A., & Ball, J. E. (1999). Application of image processing in the study of sediment motion. *Journal of Hydraulic Research*, *37*(4), 559–576.

Lajeunesse, E., Malverti, L., & Charru, F. (2010). Bed load transport in turbulent flow at the grain scale: Experiments and modelling. *Journal of Geophysical Research*, *115*, F04001–1–16.

Lee, H., & Hsu, I. (1994). Investigations of saltating particle motions. *Journal of Hydraulic Engineering*, *120*, 831–845.

Murphy, P. J., & Hooshiari, H. (1982). Saltation in water dynamics. *Journal of Hydraulic Division*, ASCE, *108*(11), 1251–1267.

Nezu, I., & Nakagawa, H. (1993). *Turbulence in open-channel flows*. Rotterdam: Balkema.

Nikora, V., McLean, S., Coleman, S., Pokrajac, D., McEwan, I., Campbell, L., . . . & Koll, K. (2007). Double-averaging concept for rough-bed open-channel and overland flows: Applications. *Journal of Hydraulic Engineering*, *133*(8), 884–895.

Niño, Y., & Garcia, M. (1994). Gravel saltation. 2. Modeling. *Water Resources Research*, *30*(6), 1915–1924.

Niño, Y., & Garcia, M. (1998). Experiments on saltation of sand in water. *Journal of Hydraulic Engineering*, ASCE, *124*(10), 1014–1025.

Niño, Y., Garcia, M., & Ayala, L. (1994). Gravel Saltation 1. Experiments. *Water Resources Research*, *30*(6), 1907–1914.

Radice, A., Malavasi, S., & Ballio, F. (2006). Solid transport measurements through image processing. *Experiments in Fluids*, *41*(5), 721–734.

Ramesh, B., Kothyari, U. C., & Murugesan, K. (2011). Near-bed particle motion over transitionally-rough bed. *Journal of Hydraulic Research*, *49*(6), 757–765.

Rickenmann, D., Turowski, J. M., Fritschi, B., Klaiber, A., Ludwig, A. (2012). Bedload transport measurements at the Erlenbach stream with geophones and automated basket samplers. *Earth Surface Processes and Landforms*, *37*, 1000–1011.

Schuyler, A., & Papanicolaou, A. N. (2000). Image analysis technique to track the evolution of sediment clusters. *Experimental Techniques*, *24*(5), 31–34.

Shvidchenko, A. B., & Pender, G. (2001). Macroturbulent structure of open-channel flow over gravel beds. *Water Resources Research*, *37*(3), 709–719.

Stewart, M. T. (2014). *Turbulence structure of rough-bed open-channel flow* (PhD Thesis). School of Engineering, University of Aberdeen, Aberdeen.

Thorne, P. D. (2014). An overview of underwater sound generated by interparticle collisions and its application to the measurements of coarse sediment bedload transport. *Earth Surface Dynamics*, *2*, 531–543.

Tsakiris, A. G., Papanicolaou, A. N., & Lauth, T. J. (2014). Signature of bedload particle transport mode in the acoustic signal of a geophone. *Journal of Hydraulic Research*, *52*(2), 185–204.

Turowski, J. M., & Rickenmann, D. (2009). Tools and cover effects in bedload transport observations in the Pitzbach, Austria. *Earth Surface Processes and Landforms*, *34*, 26–37.

Witz, M. J. (2014). *Mechanics of particle entrainment in turbulent open-channel flows* (PhD Thesis). School of Engineering, University of Aberdeen, Aberdeen.

Yalin, M. S. (1977). *Mechanics of sediment transport*. Oxford: Pergamon Press.